Applied Catalysis B: Environmental 293 (2021) 120214

Contents lists available at ScienceDirect

Applied Catalysis B: Environmental

journal homepage: www.elsevier.com/locate/apcatb

Carbon quantum dots enriching molecular nickel polyoxometalate over CdS semiconductor for photocatalytic water splitting

Yinjuan Dong [a,1], Qing Han [a,1], Qiyu Hu [a], Chunjiang Xu [a], Congzhao Dong [a], Yong Peng [d], Yong Ding [a,c,*], Yaqian Lan [b,**]

[a] State Key Laboratory of Applied Organic Chemistry, Key Laboratory of Advanced Catalysis of Gansu Province, College of Chemistry and Chemical Engineering, Lanzhou University, Lanzhou, 730000, China
[b] School of Chemistry, South China Normal University, Guangzhou, 510006, China
[c] State Key Laboratory for Oxo Synthesis and Selective Oxidation, Lanzhou Institute of Chemical Physics, Chinese Academy of Sciences, Lanzhou, 730000, China
[d] Electron Microscopy Centre of Lanzhou University, School of Physical Science and Technology, Key Laboratory for Magnetism and Magnetic Materials of Ministry of Education, Lanzhou University, Lanzhou, 730000, China

ARTICLE INFO

Keywords:
CdS
Carbon quantum dots
Enrichment effect
Polyoxometallate
Photocatalytic water splitting

ABSTRACT

An efficient and stable photocatalyst for overall water splitting is desirable for solar-energy conversion. Herein, Ni_4P_2-CQDs@CdS catalyst was obtained in situ photoreaction CQDs@CdS semiconductor composite and $[Ni_4(H_2O)_2(PW_9O_{34})_2]^{10-}$ (Ni_4P_2) polyoxometallate. Photocatalytic hydrogen evolution from pure water is realized using CdS as the light harvester, CQDs as the electron acceptor and donor and Ni_4P_2 as catalyst without addition sacrificial reagents under visible light irradiation ($\lambda = 420$ nm), which exhibits water splitting activity with H_2 evolution rate up to 145 μmol g_{cat}^{-1} h^{-1}. Experiments confirm the electrons transfer from CdS to CQDs, then to Ni_4P_2, resulting in accumulation of the electrons in Ni_4P_2 for H_2 evolution. The generated holes at the VB of CdS transfer to CQDs and oxidize H_2O to H_2O_2. The rotating ring-disk electrode test confirms the two-electron process ($2H_2O \rightarrow H_2 + H_2O_2$). This work proposes an elegant strategy for how to design multicomponent photocatalyst to realize efficient water splitting.

1. Introduction

The solar energy is regarded as the most promising energy source of producing renewable fuels for sustainable environment and energy development. Photocatalytic overall water splitting by converting solar energy into chemical fuels without using sacrificial reagents is a desired goal. Recently, semiconductor-based photocatalysts have been recognized as the most promising approach to generate carbon-free and renewable hydrogen energy [1–9]. Although tremendous efforts have been made during the past decades, an efficient photocatalyst for water splitting still encounters several challenges. Firstly, the photocatalyst should have a narrow band gap, which must exceed the high Gibbs free energy (ΔG) of water splitting (237 kJ/mol equal to 1.23 eV) but be lower than 3.0 eV in order to capture visible light efficiently [10–12] Secondly, to drive the uphill water splitting reaction, the photocatalyst should have appropriate band positions that cover the thermodynamical potentials of water redox reactions (namely conduction band (CB) $\leq$ 0 V and valence band (VB) $\geq$ 1.23 V *vs.* NHE at pH = 0, respectively) [13, 14]. The band levels usually shift with different pH (-0.059 V/pH) and the thermodynamical redox potential of water is -0.41 V *vs.* NHE at pH 7. Thirdly, the photogenerated charge carriers should be transferred and separated efficiently to inhibit their recombination [15–17]. Moreover, the photocatalyst should be durable enough against corrosion under light irradiation [18]. Therefore, developing novel catalysts and designing new photocatalytic systems for overall water splitting still have a long way in the future for this field.

Currently, photocatalytic water splitting can be achieved by employing hybrid systems with semiconductor material as solid-state light absorber assisted by noble metal or molecular catalysts [19–25]. The challenge for developing semiconductor hybrid systems depends

* Corresponding author at: State Key Laboratory of Applied Organic Chemistry, Key Laboratory of Advanced Catalysis of Gansu Province, College of Chemistry and Chemical Engineering, Lanzhou University, Lanzhou, 730000, China.
** Corresponding author.
E-mail addresses: dingyong1@lzu.edu.cn, dingyong1973@163.com (Y. Ding), yqlan@m.scnu.edu.cn (Y. Lan).
[1] These authors contributed equally to this work.

https://doi.org/10.1016/j.apcatb.2021.120214
Received 22 January 2021; Received in revised form 26 March 2021; Accepted 6 April 2021
Available online 9 April 2021

mainly on constructing H_2- and O_2-evolving cocatalysts. Simultaneous H_2- and O_2- evolution in pure water was reported using CdS nanorods decorated with Pt nanoparticulate reduction and molecular Ru-complex oxidation cocatalysts [18], which realized efficient charge separation and ultrafast electron and hole transfer to the reaction sites. Using CdSe capped with dihydrolipoic acid as light harvester in combination with a soluble molecular nickel catalyst for solar hydrogen generation in water, the H_2 evolution achieved 36 % quantum yield and exhibited impressive durability for at least 360 h [19]. This system provided good spatial charge separation via fast charge transfer from semiconductor to molecular catalyst, which was crucial to achieve high photocatalytic water splitting performance. Nevertheless, most of the publications reported the half-reactions of H_2- and O_2-evolution are at the cost of the consumption of sacrificial reagents [26–28]. Therefore, the design of new hybrid system combining semiconductor and molecular catalyst without using sacrificial reagents remains an ongoing challenge that is of significant scientific interest in artificial photosynthetic system.

Recently, carbon quantum dots (CQDs) have emerged as a relatively new class of photocatalytic materials with notable advantages, including good solar spectrum utilization, fast migration of charge carriers, excellent electron accepting and donating performances, efficient surface redox reactions and high chemical stability [29,30]. Polyoxometalates (POMs), as a large family of nanosized molecular metal oxides, undergo fast and reversible multi-electron-transfer reactions without altering their structure, thus representing excellent candidates as H_2 evolution and water oxidation catalysts [31–39]. CdS has been a hotspot for photocatalytic hydrogen production because of its narrow band-gap (≈2.4 eV) and appropriate band structure position (-1.0 ~ 2.0 V *vs*. NHE at pH = 7). Moreover, CdS meets the thermodynamic requirements for photocatalytic water splitting. However, the photocatalytic performance of CdS is seriously limited by its rapid recombination of photogenerated carriers and severe photocorrosion [40,41]. In addition, it is neccessary to replace toxid and non-sustainable Cd-based semiconductors by environmentally friendly ones.

In order to resolve the above defect of CdS, a new photocatalytic system (Ni_4P_2-CQDs@CdS) was constructed using CdS as light harvester, CQDs as the electron acceptor and donor, in combination with a molecular Ni-containing POM catalyst of $[Ni_4(H_2O)_2(PW_9O_{34})_2]^{10-}$ (Ni_4P_2), which can be used for pure-water splitting to simultaneous generation H_2 and H_2O_2 without the assistance of additional sacrificial reagents under visible light irradiation (λ = 420 nm). The result shows that the electrons transfer from CdS to CQDs and then to Ni_4P_2, making electrons accumulate in Ni_4P_2 for H_2 evolution. The generated holes at the VB of CdS transfer to CQDs, and oxidize H_2O to produce H_2O_2. This work provides a new insight in design the novel efficient multicomponent photocatalysts for overall water splitting.

2. Experimental section

2.1. Materials

All salts and other chemicals were of the highest purity available from commercial sources without further purification. Purified water (18.25 MΩ cm applied in all the experiments was attained from a Molecular Lab Water Purifier.

2.2. Synthesis of $Na_6K_4[Ni_4(H_2O)_2(PW_9O_{34})_2]\cdot 32H_2O$ (Ni_4P_2)

Ni_4P_2 POM was synthesized according to modified literature method as follows [42]: $Na_2WO_4\cdot 2H_2O$ (16.5 g, 50 mmol) and Na_2HPO_4 (0.78 g, 5.5 mmol) were dissolved in 50 mL pure water with the pH adjusted to 7.0 using concentrated acetic acid. A solution of $Ni(OOCCH_3)_2\cdot 4H_2O$ (2.75 g, 11 mmol) in 25 mL pure water was added slowly to mixture with vigorous stirring. The resulting mixture was refluxed for 2.5 h and filtered hot to remove any precipitate, then 2 g of $K(OOCCH_3)$ was added and the hot yellow solution left for crystallization. A mixture of small yellow high quality crystals and crystalline powder of the desired products was collected by filtration with high yield (11 g, 73 %). The sample Ni_4P_2 was analyzed by elemental analysis. Elemental analysis for Ni_4P_2: calculated for Na, 2.46; K, 2.79; Ni, 4.19; P, 1.11; W, 59.08 %; found for Na, 2.39; K, 2.81; Ni, 4.23; P, 1.18; W, 57.81 %.

2.3. Preparation of CQDs@CdS composite

CQDs@CdS was prepared by simply mixing an aqueous solution of CdS (10 mg) with CQDs solutions of various mass (1, 2, 3, 5 mg) in 1 mL pure water. The obtained samples were denoted as 9.1 %-CQDs@CdS, 16.7 %-CQDs@CdS, 23.1 %-CQDs@CdS, and 33.3 %-CQDs@CdS, respectively, where the prefixes indicate the theoretical weight percentage of CQDs in the CQDs@CdS hybrids. Typically, the material used for characterizations and photocatalytic tests were the 16.7 %-CQDs@CdS sample (CQDs@CdS for clarity) unless otherwise stated.

2.4. Preparation of Ni_4P_2-CQDs@CdS composite

A suspension of 10 mg of CQD@CdS and 1–5 mg of Ni_4P_2 was added into 15 mL pure water, then the resulted mixture was irradiated by LED light source (100 mW cm^{-2}, λ = 420 nm) under continuous stirring. After illumination, the resulting products were separated by centrifugation, washed with ultrapure water and dried at 60 °C for 8 h.

2.5. Photocatalytic water splitting test

The photocatalytic water splitting tests were carried out in a glass reactor sealed with a rubber septum with constant stirring at room temperature. Typically, photocatalytic reaction was performed in 15 mL pure water containing CQD@CdS (10 mg) and the Ni_4P_2 (1–5 mg) (the total volume of the flask was 21 mL). The above solution was capped and deoxygenated by purging with Ar gas for 15 min to remove the air. The reaction was then started by irradiating the solution with a LED light source (Beijing Perfectlight, PLS-LED100B, 100 mW cm^{-2}, λ = 420 nm) at room temperature. After each sampling time, 100 μL of Ar was injected into the flask and then the same volume of gas sample in the headspace of the flask was withdrawn by a SGE gas-tight syringe and analysed by gas chromatography (GC). The H_2 in the sampled gases were separated by passing through a 2 m × 3 mm packed molecular sieve 5 Å column with an Ar carrier gas and quantified by a thermal conductivity detector (TCD) (Shimadzu GC-9A). The total amounts of evolved H_2 were calculated based on the concentrations of H_2 in the headspace gas.

2.6. Detection of hydrogen peroxide (H_2O_2)

An iodometric method was used to calculate the production of H_2O_2. Typically, the irradiated suspension was filtered by a filter head to remove the catalyst after the hydrogen detection, which could be able to suppress the UV absorption background of the catalyst. Besides, to prepare the standard solution for H_2O_2 detection, 809.7 mg of potassium iodide and 15.1 mg ammonium molybdate tetrahydrate were added into 50 mL pure water under continuous stirring. Afterward, 50 μL of standard solution was added into 5 mL of the filter liquor, which turned the dispersion to yellow. Then the mixed liquor made to stand for a long time, and the absorbancy of iodine in 352 nm was applied to obtain its concentration by using a UV–vis spectrophotometer. Finally, the amount of H_2O_2 generated was evaluated by peak area of UV–vis absorption using calculated standard curve.

2.7. Detection of electron transfer number

The electron transfer number was determined via a rotating disk-ring electrodes (RRDE) testing system (RRDE-3A, ALS Co. Ltd). RRDE experiments were performed in Ar saturated 0.1 M KPi buffer (pH 7) (rotating speed: 1600 rpm; scan rate: 10 $mV\cdot s^{-1}$). A CHI 760D

workstation (CH Instruments Co.) was implemented to record the data. The RRDE consists of a glassy carbon disk (r1 = 4 mm), an insulator ring (r2 = 5 mm), and a glassy carbon ring (r3 = 7 mm).

For preparing RRDE measurements, 1 mg of Ni_4P_2-CQDs@CdS sample and 20 μL of 0.5 % Nafion (DuPont) were uniformly dispersed in 1 mL of water/ethanol (volume ratio: 1/1) mixture solution. Subsequently, the mixture was treated under ultrasonication for 1 h to get the homogeneous suspension. Whereafter, 10 μL of suspension was drop-cast onto the disk electrode. Pt plate and Ag/AgCl electrode (3.5 M KCl) were used as counter and reference electrodes, respectively. 0.1 M KPi buffer (pH 7) was employed as an electrolyte after saturation with Ar gas for 30 min.

2.8. EPR measurement

$\cdot O_2^-$ radicals were measured using electron paramagnetic resonance (EPR) spectroscopy in the photocatalytic reaction system under LED light source (100 mW cm^{-2}, λ = 420 nm), in which the $\cdot O_2^-$ radicals can be captured by 5,5-dimethyl-1-pyrroline N-oxide (DMPO). Before determining the superoxide radicals (DMPO-$\cdot O_2^-$, an EtOH/water (v/v = 9/1) mixture (5 mL) was photoirradiated with CQDs@CdS (15 mg) and Ni_4P_2 (3 mg) and DMPO (0.1 mmol).

3. Results and discussion

3.1. The designment of three components reaction system of Ni_4P_2-CQDs@CdS

The three component reaction system of Ni_4P_2-CQDs@CdS was obtained by physical mixture of CQDs@CdS semiconductor composite and Ni_4P_2 for direct reaction in pure water (Scheme 1). In photocatalytic process, once the photocatalytic reaction starts, the CQDs@CdS semiconductor composite will combine with Ni_4P_2 POM catalyst due to the enrichment effect of CQDs to Ni_4P_2. This is the first report of CQDs enriching Ni_4P_2 POM over semiconductor for water splitting. The photocatalytic hydrogen evolution from pure water is successfully realized using CdS as the light harvester, CQDs as the electron acceptor and donor, and Ni_4P_2 as catalyst under visible light irradiation. Ni_4P_2 as catalyst was obtained from salts of earth-abundant elements (nickel acetate, sodium tungstate, and Na_2HPO_4) following modified literature [42] and systematically characterized by elemental analysis for the synthesis of Ni_4P_2 and FT-IR (Fig. S1). After aging 3 h, no apparent changes of the UV–vis spectra are observed in water, which indicates that Ni_4P_2 possesses good hydrolytic stability (Fig. S2).

3.2. Characterization of CQDs@CdS semiconductor composite

The CQDs@CdS hybrid was synthesized through an impregnation strategy, namely, the surface of CdS was uniformly loaded with CQDs by electrostatic interaction in deionized water. The FT-IR spectra of the CQDs@CdS composite as well as those of the free components CdS and CQDs are shown in Fig. 1a. The strong characteristic peaks located at 1383 and 1566 cm^{-1} are assigned to the typical symmetric and asymmetrical stretching modes of the carboxylate group derived from the surface of CQDs, respectively [43]. Significantly, the peaks are shifted from that of pure CQDs (the carboxylate group stretches; ν = 1390 and 1570 cm^{-1}), which results from the incorporation of the CQDs on the surface of CdS. Additionally, the vibration band from CdS for CQDs@CdS composite can hardly be observed due to the weak infrared stretching vibration. The positive zeta potential values (ζ, 0 ~ 12 mV) are associated with CdS nanorods (NRs), while negative zeta potential values (ζ, 0 ~ −55 mV) are obverved over CQDs (Fig. 1b and Fig. S3−4), which suggests the presence of electrostatic interaction between CQDs and CdS NRs. The CQDs@CdS composite exhibits similar XRD patterns of CdS, suggesting that the crystalline structure of CdS [44] is retained after incorporating CQDs (Fig. S5). No characteristic diffraction peaks of CQDs [45,46] are observed in the CQDs@CdS, which may be ascribed to the relatively low loading weight, the high dispersion as well as the overlapping of peaks for (002) plane of CdS in the same position.

From thermogravimetric analysis (TGA) of CQDs@CdS (Fig. S6), the first weight loss (0.6 %) in the range from 25 to 198 °C is assigned to the liberation of surfaces water molecules. The second loss (1.8 %) in 198−600 °C region is concerned with the decomposition of CQDs. Furthermore, in the C 1s X-ray photoelectron spectroscopy (XPS) of CQDs@CdS composite (Fig. 1c). The peak centered at 284.8 eV is ascribed to sp^2 C-C, and those peaks centered at 286.3 and 288.4 eV represent C-O and C = O, respectively [47]. The morphology of the CQDs@CdS composite was analyzed by the scanning electron microscopy (SEM) and transmission electron microscopy (TEM). The CQDs@CdS exhibits rod-like 1-D morphology (Fig. 1d-e). The magnified TEM images of the circles highlighted in Fig. 1f and Fig. S7 reveal the CQDs with the same size (about 7 ± 2 nm). As indicated by the white circles, the CQDs are distributed on the whole CdS NRs. EDX elemental mapping (Fig. 1g) results of CQDs@CdS show Cd, S, C, and O elements'

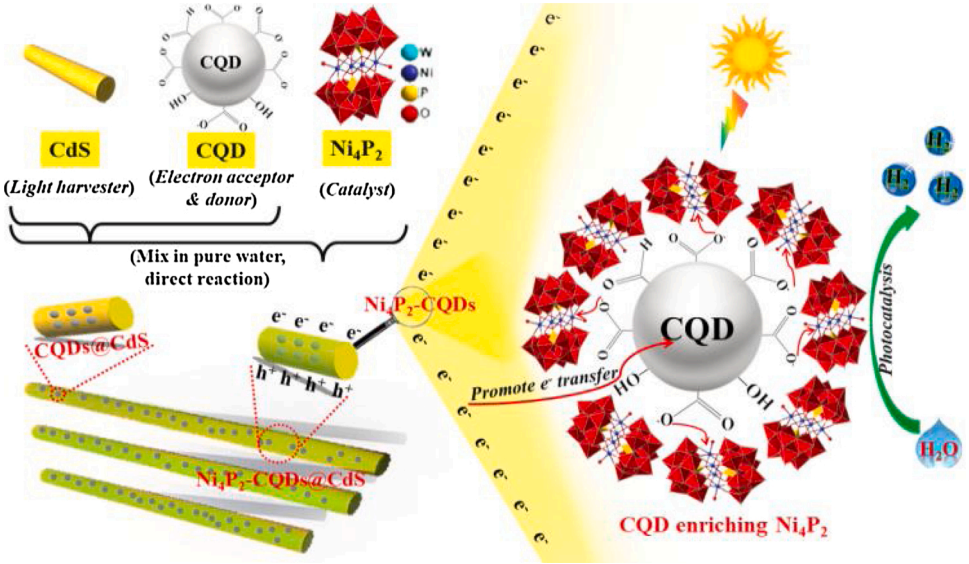

Scheme 1. Photocatalytic water splitting over the hybrid Ni_4P_2-CQDs@CdS system.

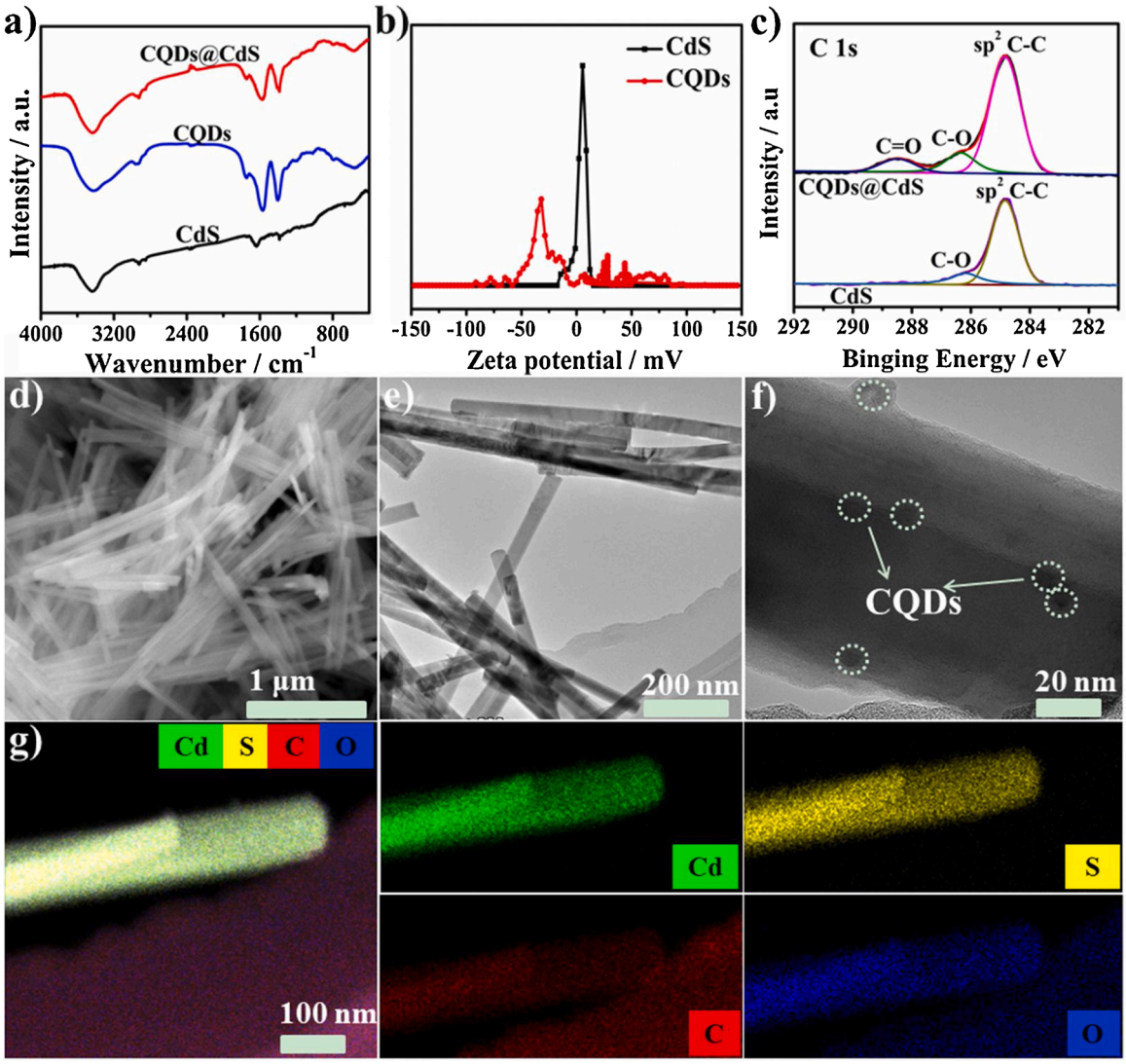

Fig. 1. a) FT-IR spectra and b) Zeta potential distribution of CdS and CQDs. c) High-resolution XPS spectra of C 1s for pure CdS and CQDs@CdS. d) SEM and e) TEM images of CQDs@CdS. f) Magnified TEM image corresponding to the area highlighted in (f) CQDs are marked with white circles. g) TEM image of CQDs@CdS and corresponding EDX elemental mappings of Cd, S, C and O.

signals, demonstrating uniform dispersion of CQDs at the surface of CdS NRs.

CQDs are obviously attached to the surface of CdS NRs (Fig. 2a-b) and CQDs have a great influence on the charge distribution (Fig. S8). After the modification of CQDs, the surface charge difference is significantly increased. And a large energy band bend on the upper surface is formed, which effectively promotes charge carriers separation (Fig. 2c). The steady-state photoluminescence (PL) spectra and time-resolved PL spectroscopy were conducted to probe the recombination efficiency of photoinduced electrons and holes. The intensity steady-state PL spectrum at 520 nm of CQDs@CdS is much weaker than that of pure CdS catalyst (Fig. 2d), demonstrating that the recombination of light-excited electrons and holes is more effectively prohibited in CQDs@CdS. CQDs@CdS exhibits a longer average lifetime of 1.66 ns than that of bare CdS (1.47 ns) (Fig. 2e and Fig. S9). The lifetime increase of CQDs@CdS indicates that the incorporation of CQDs over CdS can effectively suppress the charge carriers recombination between CQDs and CdS and increase the lifetime of charge carriers [48,49]. The above results demonstrate the existence of a strong interaction between CdS and CQDs in CQDs@CdS, which is highly favorable for efficient charge-separation/transfer in the hybrid, further improving the photocatalytic performances of CQDs@CdS [50,51].

3.3. Photocatalytic water splitting activity of Ni_4P_2-CQDs@CdS

As the optical property of catalyst plays a key role in determining the photocatalytic activity, UV–vis diffuse reflectance spectra (DRS) measurement was performed to study the photoabsorption property of the as-prepared samples (Fig. 3a). Compared with pure CdS with an absorption edge at about 516 nm [52] CQDs@CdS has no apparent shift in the absorption edge, suggesting that CQDs are not incorporated into the CdS lattice but loaded on the CdS surface, which is consistent with that of XRD result.

In order to confirm the relative optical band gap of CdS semiconductor, the band gap energy (E_g) is estimated from the Kubelka – Munk equation: $\alpha(h\nu)=A(h\nu-E_g)^{0.5}$ (where α, ν, h, A, and E_g are absorption coefficient, light frequency, Planck's constant, constant value, and band gap energy, respectively) [52]. As shown in Fig. S10, the optical band gap of bare CdS is calculated to be about 2.41 eV from the plot of $(\alpha h\nu)^{1/2}$ versus $(h\nu)$, which is consistent with the reported value [44]. Besides, Mott – Schottky plot of the CdS is collected to define its CB positions (Fig. S11). The derived flat-band potential of CdS is about -0.53 (*vs.* Ag/AgCl). It is generally known that the bottom of the conduction band of n-type semiconductor is more negative by ≈0.20 eV than the flat band potential. Therefore, the conduction band (CB)

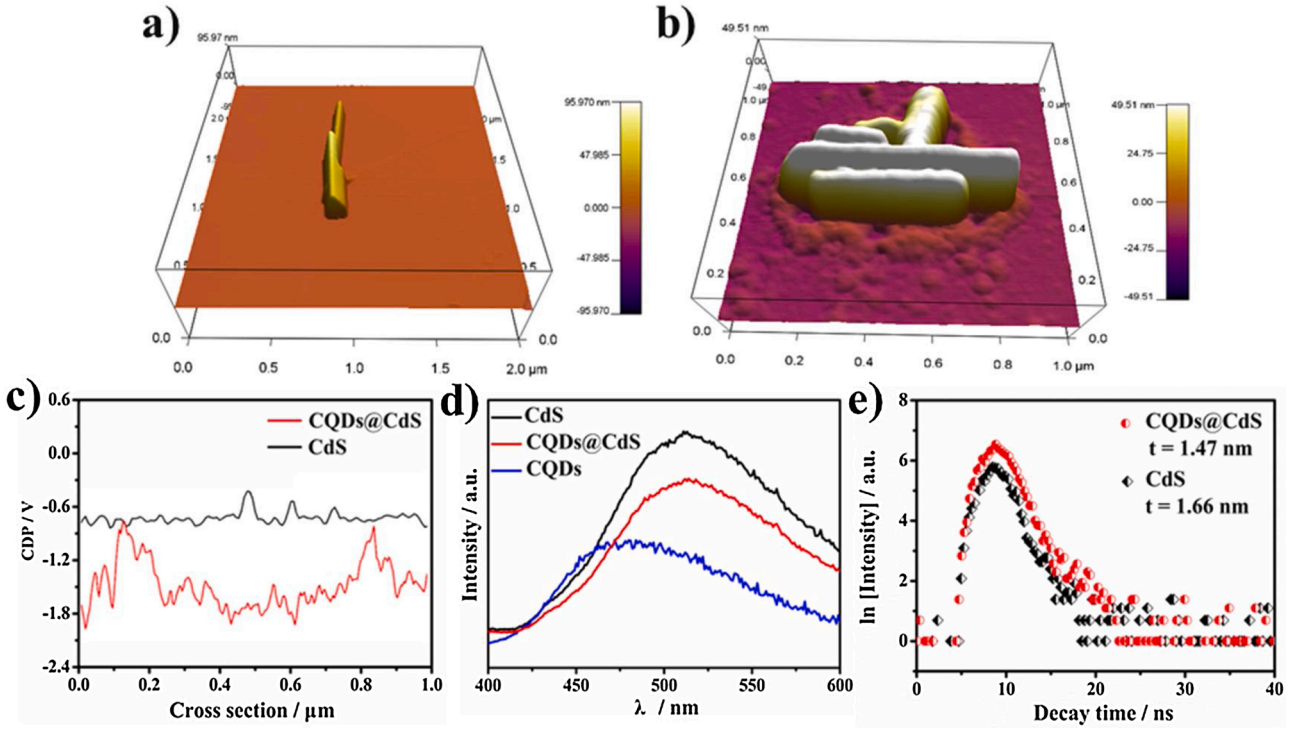

Fig. 2. a) AFM topographic image of CdS. b) AFM topographic image of CQDs@CdS. c) Cross-sections of the surface potential images of CdS and CQDs@CdS. d) Steady-state PL spectra of CdS, CQDs, and CQDs@CdS under 400 nm excitation. e) Time-resolved PL spectra of the samples at corresponding steady-state emission peaks of CdS and CQDs@CdS.

potentials of CdS is estimated to be ~−0.73 eV, that is -0.53 eV *vs.* normal hydrogen electrode (NHE) ($E_{NHE} = E_{Ag/AgCl} + E^{\theta}_{Ag/AgCl}$; $E^{\theta}_{Ag/AgCl} = 0.1976$ V) [53]. Considering the E_g value of 2.41 eV has been estimated from the UV–vis DRS (Fig. S10), the VB should be located at 1.88 eV (*vs.* NHE). Therefore, the band structures of CdS endow the proper ability for water splitting.

Additionally, Ni_4P_2 shows strong absorption in all region (Fig. 3a), from which the band gap (E_g) can be determined to be 2.51 eV (Fig. S12), indicating that it displays semiconductor-like properties. The CV curve of Ni_4P_2 (Fig. 3b) presents two reversible redox couples, both of which corresponds to a one electron redox process. Upon scanning to a more negative potential, the CV has large and irreversible reductive wave peak with an onset potential of -1.38 V. These electrochemical behaviors indicate that the Ni_4P_2 can act as the catalyst for proton reduction after the acceptance of three electrons [54].

The pure water splitting performance of the as-obtained samples without any sacrificial reagents or noble metals, or other additives under visible light irradiation (λ = 420 nm) were investigated. We conducted separate light-driven water splitting experiments in the absence of one or two of the three components (Ni_4P_2, CQDs, and CdS). No H_2 or O_2 was detected after 17 h irradiation, revealing that all of the three components are essential for the water splitting reaction (Fig. 3c). The bare CdS sample is almost inactive because of the high recombination rate of photoexcited charges. Under appropriate conditions, a high H_2 formation rate of 145.0 μmol g_{cat}^{-1} h^{-1}, turnover frequency of 15.5 h^{-1} and apparent quantum efficiency ~0.57 % at 420 nm are obtained when the mass of CdS@CQDs, Ni_4P_2 are 10 and 2 mg, respectively, which indicates that the mass ratio of the three components in the hybrid greatly affect the catalytic performance (Fig. 3d and Fig. S13). Such a noble-metal-free H_2 generation rate is comparable to that of other works reported (Table S1). Durability testing for the photocatalytic water splitting of Ni_4P_2-CQDs@CdS is shown in Fig. 3e. The solid photocatalyst is removed from the solution after 48 h reaction and the liquid phase is allowed to react under the same photocatalytic reaction conditions. We do not detect H_2 evolution for the filtrate sample after 48 h reaction. The trends of the hydrogen generation activity on the tested Ni_4P_2-CQDs@CdS photocatalyst are generally consistent with their incident light intensity (Fig. S14).

Polyoxometalates (POMs) usually show reversible multi-electron redox feature, which has great potentialities for diverse photocatalytic applications. We compare the photocatalytic performance of Ni_4P_2 with other POMs and $Ni_2(Ac)_2$ catalysts under the same reaction conditions and find that $Ni_2(Ac)_2$ and NiSi POM have poor activity, while Co-, Cu-, Fe-based POM catalysts have no activity (Fig. 3f). When CdS is replaced with other semiconductors (such as g-C_3N_4 and TiO_2, Fig. S15−16), no hydrogen is detected. Whereas, when CQDs with different sizes were investigated, activities of three reactions are comparable (Table 1).

3.4. *Detection of H_2O_2 and electron transfer number over Ni_4P_2-CQDs@CdS*

To further explore the whereabouts of photogenerated holes, we tested what kind of oxidative product (O_2 or H_2O_2) was formed in the Ni_4P_2-CQDs@CdS system. No O_2 was detected in the photocatalytic reaction progressing, which is maybe due to the weak oxidation capacity of the holes [41]. However, a small amount of H_2O_2 (0.45 μmol H_2O_2 for 3 h) was detected by an iodometric method (Fig. 4a and Fig. S17a-b). The molar ratio of H_2 and H_2O_2 is close to 1:1, indicating the electron/hole utilization ratio is equal, which is an important symbol of overall water splitting. As shown in Fig. S17c, nearly no H_2O_2 is produced over CdS due to the rapid recombination of photogenerated carriers. Similarly, no H_2O_2 is produced over Ni_4P_2-CdS, indicating h^+ can not transfer from CdS to Ni_4P_2. However, CQDs@CdS produces trace amount of H_2O_2, suggesting CQDs can accelerate h^+ transport. CQDs, CQDs@CdS and Ni_4P_2-CQDs are capable of producing H_2O_2, indicating that CQDs participate in the photocatalytic reaction as H_2O-to-H_2O_2 reaction sites.

H_2O_2 is one of the most important fundamental chemicals in the modern chemical engineering industry as well as energy and environmental applications. The two-electron water oxidation is a promising

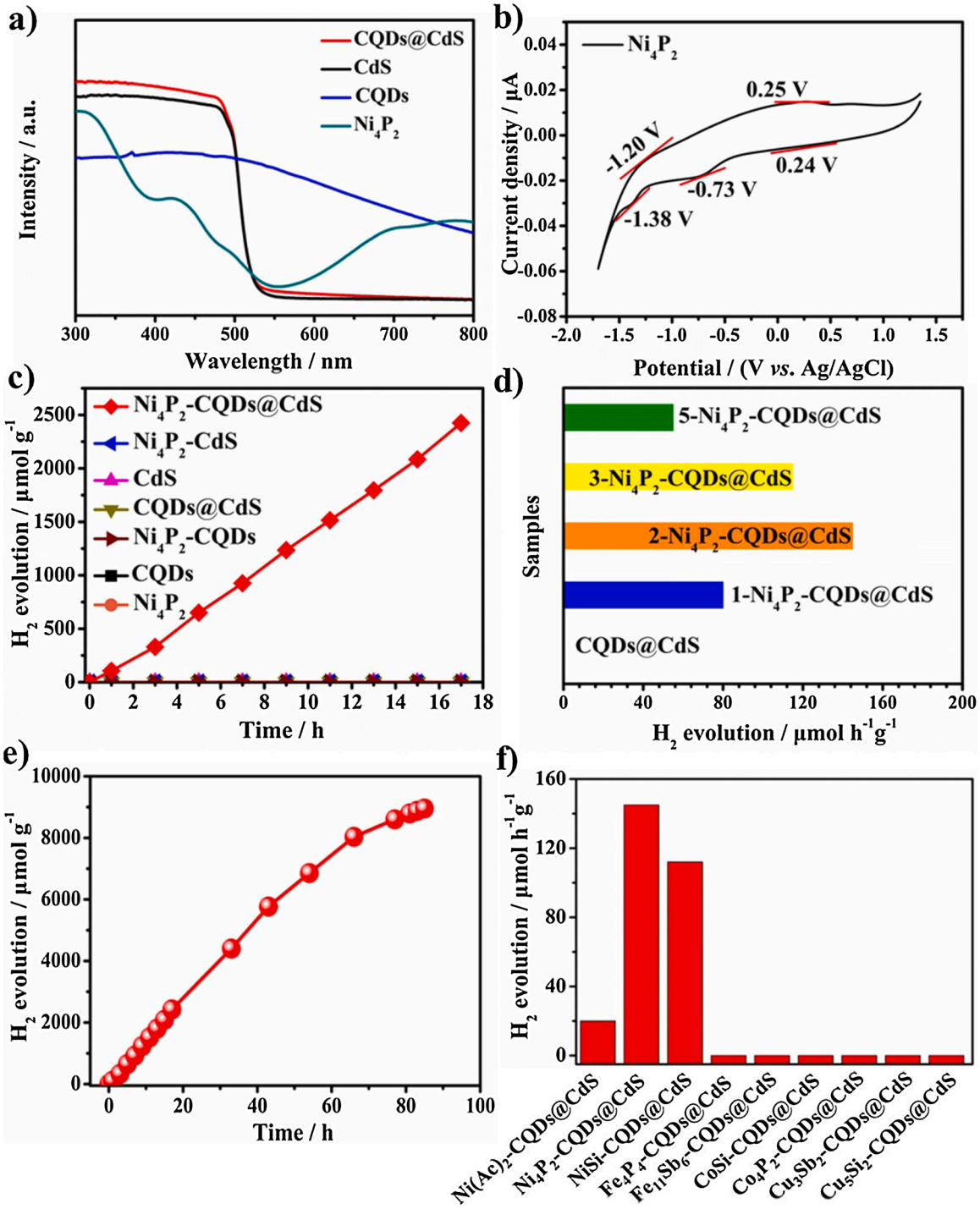

Fig. 3. a) UV–vis DRS spectra of CdS, CQDs, Ni_4P_2 and CQDs@CdS. b) Cyclic voltammetry (CV) of 1 mM Ni_4P_2 in pure water with a scan rate of 100 mV s^{-1}. c) Time course of water splitting in pure water by different photocatalysts. d) Photocatalytic water splitting performance of Ni_4P_2-CQDs@CdS with different Ni_4P_2 mass (0, 1, 2, 3, 5 mg). The prefixes indicate the actual weight (mg) of Ni_4P_2 in the Ni_4P_2-CQDs@CdS hybrids. e) Durability testing for the photocatalytic water splitting of three component system of Ni_4P_2-CQDs@CdS. f) Photocatalytic water splitting performance using different POM catalysts with CQDs@CdS composite. Reaction conditions: 15 mL of pure water, illumination with 420 nm LED lamp (100 mW cm^{-2}), vigorous agitation using a magnetic stirrer.

route for H_2O_2 generation [57]. Here, the rotating ring-disk electrode (RRDE) system was used to detect electron transfer number over Ni_4P_2-CQDs@CdS during water splitting process. The disk current represents the oxidation of H_2O, in which water can be oxidized to O_2 with $4e^-$ transfer product or H_2O_2 with $2e^-$ transfer product. The value of ring current represents the amount of H_2O_2 generated on the disk electrode [58]. I–t curve was measured via rotating disk electrodes (RDE) test at a rotation rate of 1600 rpm (Fig. 4b), which exhibits a time-course downward sloping because of the successive consumption of H_2O_2. In addition, the current shows a sharp increase when the rotation of RDE was turned on. This phenomenon indicates the rotation of RDE promotes the diffusion of H_2O_2 [59].

The number of transferred electron (n) involved in the reaction is quantified by the RRDE i–t collection experiment (Fig. 4c) operated at a rotation rate of 1600 rpm. The current obviously increases when the reaction is illuminated. Further, electron transfer number (n) and H_2O_2

Table 1
Comparison of the H_2 evolution reaction activity by different catalysts[a].

Entry	Semiconductor composite	Catalyst	H_2 (μmol g_{cat}^{-1} h^{-1})
1	CQDs@CdS	$H_3PW_{12}O_{40}$	0
2[b]	CQDs@g-C_3N_4	Ni_4P_2	0
3[c]	CQDs@Meso-TiO_2	Ni_4P_2	0
4[d]	CQDs@CdS	Ni_4P_2	140
5[e]	CQDs@CdS	Ni_4P_2	72
6	CQDs@CdS	Ni_4P_2	145

[a] Conditions: LED lamp (λ = 420 nm, 100 mW cm^{-2}), semiconductor composite (10 mg), catalyst (2 mg), 15 mL H_2O, reaction for 3 h. Total reaction volume 15 mL, vigorous agitation using a magnetic stirrer.
[b] g-C_3N_4 was prepared by calcination according to a literature [55].
[c] Meso-TiO_2 was synthesized according to the method described in the literature [26].
[d] CQDs was prepared using a modified literature procedure [28], where the diameter of CQD is.2–6 nm.
[e] CQDs was synthesized according to our previously reported method [56], where the average diameter of CQD is 10 nm.

yield are calculated according to the following Eqs. (1) and (2) [60]:

$$n = 4I_{disk}/(I_{disk}+I_{ring}/N) \quad (1)$$

$$H_2O_2 \text{ yeild } (\%) = 2I_{ring}/(N*I_{disk}+I_{ring}) \quad (2)$$

Where, I_{disk} and I_{ring} represent the disk and ring currents, respectively. N is the RRDE collection efficiency determined to be 0.353.

The electrons transfer number of 1.93 and the H_2O_2 yield of 94 % are obtained, indicating that the photocatalytic water splitting with Ni_4P_2-CQDs@CdS is a two-electron process ($2H_2O \rightarrow H_2 + H_2O_2$). Furthermore, the investigation of $\cdot O_2^-$ active specie was executed by electron paramagnetic resonance (EPR) spectroscopy with 5,5-dimethyl-1-pyrroline N-oxide (DMPO) as a spin-trapping reagent (Fig. 4d). It is finding that no EPR signal is detected in the dark, but the characteristic signals of the DMPO-$\cdot O_2^-$ is observed under light, further confirming the production of H_2O_2 during the photocatalytic process over Ni_4P_2-CQDs@CdS.

3.5. Enrichment effect of CQDs to Ni_4P_2 POM

After the light reaction, the SEM and TEM images of Ni_4P_2-CQDs@CdS exhibit a relatively rough surface compared with these of CQDs@CdS and Ni_4P_2-CdS (Fig. 5a and Fig. S18−22). To further explore the surface structure variations of CQDs@CdS after the introduction of Ni_4P_2, high resolution TEM measurements were performed (Fig. 5b-c). For Ni_4P_2-CQDs@CdS sample, a uniform amorphous thin-layer with a thickness of ~5 nm is evidently observed (Fig. 5c), indicating the formation of ultrathin Ni_4P_2 nanolayers on the surfaces of CQDs@CdS. Meanwhile, the energy dispersive spectroscopy (EDS) elemental line scanning (Fig. 5d and Fig. S23), elemental mapping results (Fig. S24) and EDX spectrum (Fig. S25) confirm that the uniform dispersion of Ni_4P_2 layers on the surface of CQDs@CdS. Accordingly, the TEM-EDS (Fig. S26) and elemental mapping (Fig. S27) of Ni_4P_2-CdS show the signal of Ni and P is relative weak. These findings show the CQDs@CdS semiconductor composite will combine with Ni_4P_2 molecular catalyst

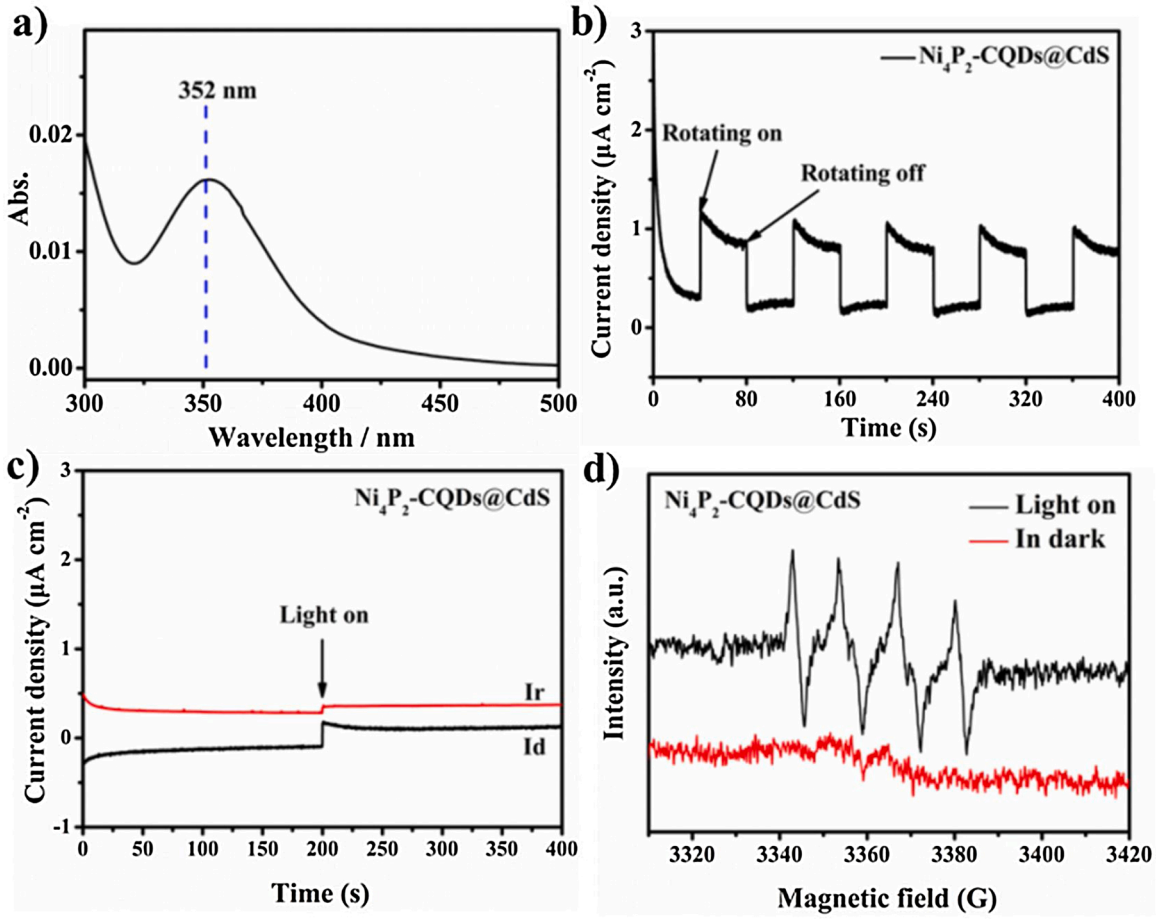

Fig. 4. a) UV–vis absorption spectra for Ni_4P_2-CQDs@CdS system after 3 h light irradiation and centrifugation by adding potassium iodide solution and ammonium molybdate tetrahydrate solution. b) I–t curve of Ni_4P_2-CQDs@CdS with or without rotating at a rotation rate of 1600 rpm. c) I–t curves of Ni_4P_2-CQDs@CdS using RRDE under dark or light at a rotation rate of 1600 rpm d) DMPO spin trapping EPR technique to measure $\cdot O_2^-$ generated photoreaction over Ni_4P_2-CQDs@CdS under dark or light.

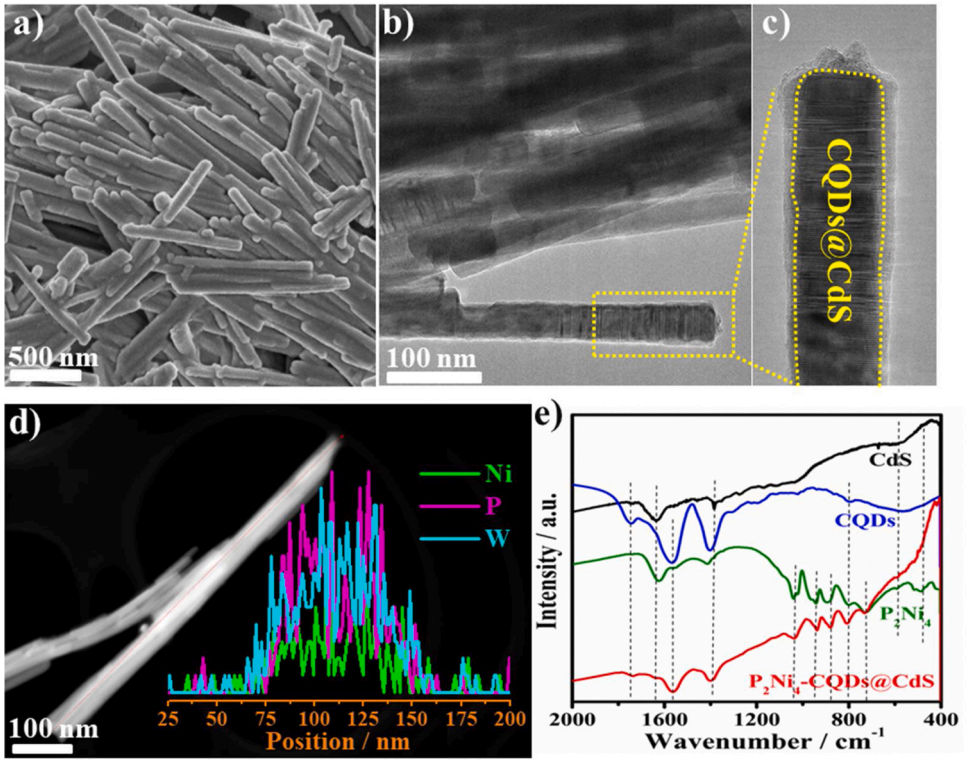

Fig. 5. a) SEM image, b, c) TEM images, and d) TEM-EDS line analysis of Ni_4P_2-CQDs@CdS. e) IR spectra of CdS, CQDs, Ni_4P_2 and Ni_4P_2-CQDs@CdS in the range of 2000-400 cm^{-1}.

once the photocatalytic reaction starts due to the enrichment effect of CQDs to Ni_4P_2. The FT-IR spectrum of the Ni_4P_2-CQDs@CdS composite clearly gives the characteristic peaks of CdS, CQDs and Ni_4P_2 free components, which is further justified CQDs enriching Ni_4P_2 (Fig. 5e and Fig. S28). The possible photocatalyst leaching in terms of carbon quantum dots or metal counterparts from the solid to the liquid phase after prolonged irradiations for 48 h is analysed by ICP-AES, TEM and UV–vis (Fig. S29−30).

To further clarify the enhanced H_2 activity of CQDs@CdS owing to the enrichment effect of CQDs to Ni_4P_2 POM, the inductively coupled plasma atomic emission spectrometry (ICP-AES) was employed to measure the Ni content (Table 2). It can be seen that the ICP-AES test value of Ni_4P_2-CQDs@CdS after irradiation for 17 h is close to that of theoretical Ni content of Ni_4P_2-CQDs@CdS, indicating that CQDs@CdS can continuously enrich Ni_4P_2 POM with increasing irradiation time.

Furthermore, the surface topography and the surface potential images of as-obtained samples are shown in Fig. 6. To clearly compare the surface potential change of Ni_4P_2-CQDs@CdS samples, surface photovoltage (SPV) test was executed (Fig. 6c and 6f). The SPV image is obtained by subtracting the illuminated potential image with that in the dark. The SPV image of the obtained Ni_4P_2-CQDs@CdS sample without illumination shows a 90 mV change under 450 nm excitation. Inversely, the SPV image of the obtained Ni_4P_2-CQDs@CdS sample with illumination exhibits a significant change of 140 mV under 450 nm excitation. Combination ICP-AES and SPV tests, the results demonstrate enriching more Ni_4P_2 POM leads to more obviously charge separation effect for Ni_4P_2-CQDs@CdS composite. The more positive SPV is observed, the higher concentration of photogenerated holes is reflected. The strong charge separation ability of Ni_4P_2-CQDs@CdS will finally enhance the oxidation ability of CdS with high concentration of photogenerated holes and further leave the free electrons in the Ni_4P_2 POM to generate H_2 [61].

Table 2
Comparison of element content by ICP-AES for recovered sample under different reaction conditions[a].

Entry	Semiconductor composite	Ni content (wt %)	Reaction condion
1	Ni_4P_2-CQDs@CdS	0.03 %	Stirring 3 h without illumination
2	Ni_4P_2-CQDs@CdS	0.31 %	Illumination 3 h
3	Ni_4P_2-CQDs@CdS	0.56 %	Illumination 17 h

[a] Conditions: LED lamp (λ = 420 nm, 100 mW cm^{-2}), CQDs@CdS (10 mg), Ni_4P_2 (2 mg), 15 mL H_2O. Total reaction volume 15 mL, vigorous agitation using a magnetic stirrer. After centrifugation, the ICP-AES test was carried out.

3.6. Exploration of electron transfer direction and mechanistic insight

The electronic states of the elements in Ni_4P_2-CQDs@CdS were studied by XPS. The binding energies of Cd 3d and S 2p (Fig. 7a-b) over Ni_4P_2-CQDs@CdS are positively shift compared to those of in CQDs@CdS and CdS, indicating that the Cd and S on the Ni_4P_2-CQDs@CdS surface act as a kind of electron donor state [62]. Compared with that of Ni_4P_2, the binding energies of Ni 2p (Fig. 7c) over Ni_4P_2-CQDs@CdS are negatively shifted by 0.50 eV, which is attributed to the increase in electronic density in CQDs@CdS after introducing Ni_4P_2 and the presence of strong interaction between CQDs@CdS and Ni_4P_2 POM [63].

Furthermore, to prove the electrons transfer direction, seven separate experiments were performed for H_2 evolution half-reaction using triethanolamine as a hole scavenger under LED lamp irradiation (Fig. 8a). It is found that the order of hydrogen evolution rates is CQDs@CdS < CdS < Ni_4P_2-CdS < Ni_4P_2-CQDs@CdS, and separate Ni_4P_2, CQDs and Ni_4P_2-CQDs have no hydrogen evolution activity, confirming that electron transfer from CdS to CQDs, and then to Ni_4P_2, as well as subsequent proton reduction. The accelerated charge transport kinetics over Ni_4P_2-CQDs@CdS is reflected by the increased current response in transient photocurrent spectra (Fig. 8b). The reduced semi-

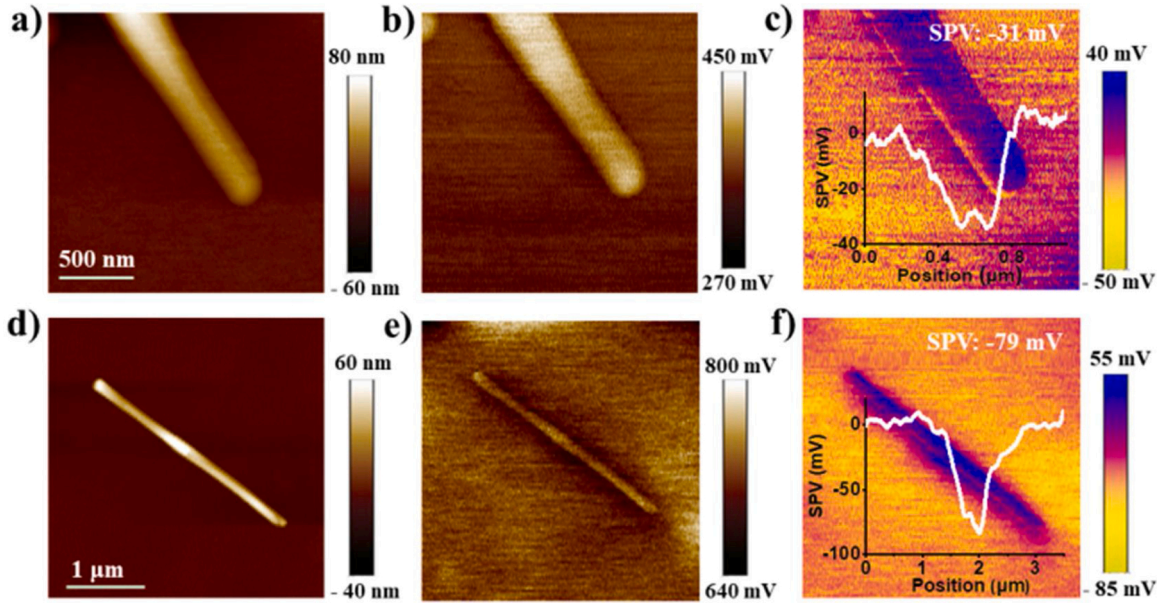

Fig. 6. (a) AFM images, (b) surface potential image and (c) SPV image under 450 nm excitation of the obtained Ni_4P_2-CQDs@CdS without illumination. (d) AFM images, (e) surface potential image and (f) SPV image under 450 nm excitation of the obtained Ni_4P_2-CQDs@CdS with illumination.

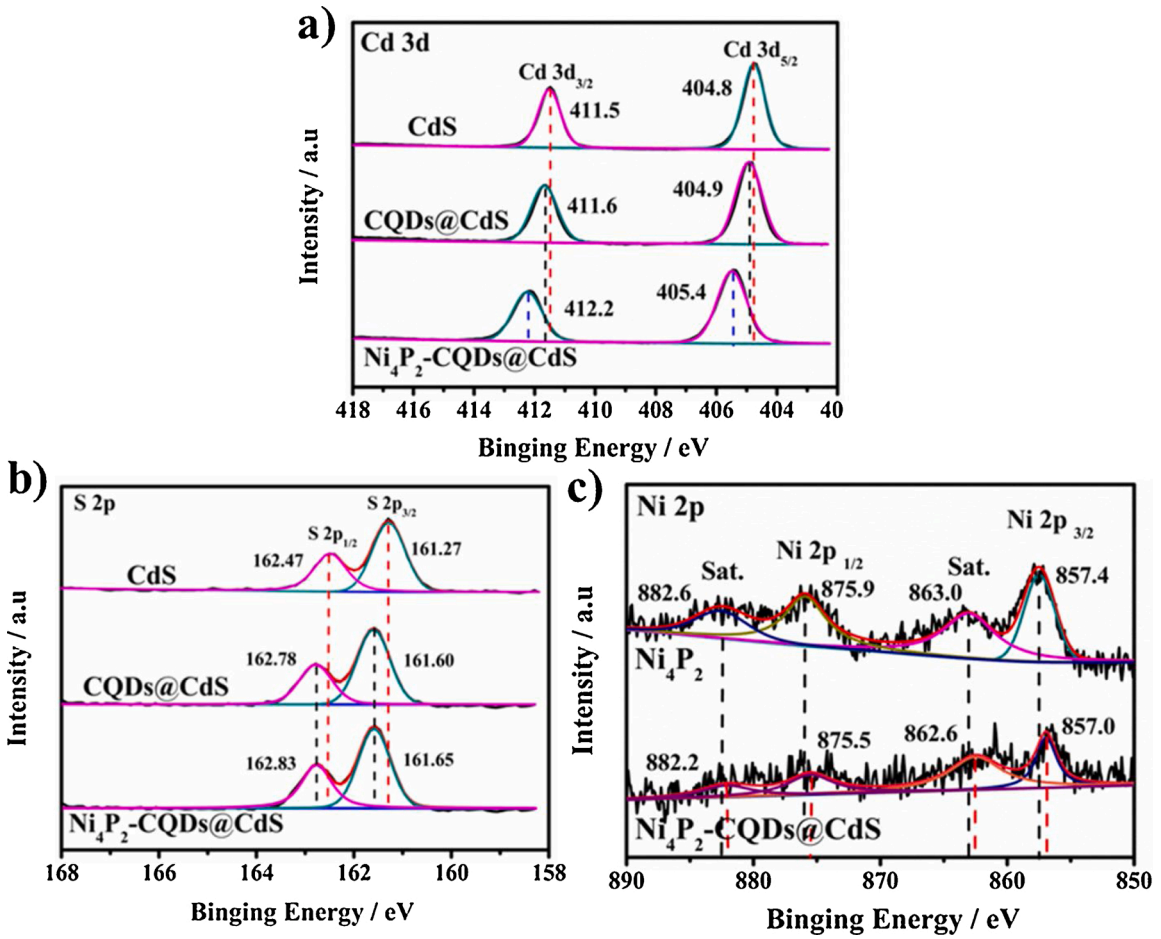

Fig. 7. a) High-resolution XPS spectra of Cd 3d and b) High-resolution XPS spectra of S 2p for pure CdS, CQDs@CdS and Ni_4P_2-CQDs@CdS. c) High-resolution XPS spectra of Ni 2p for pure Ni_4P_2 and Ni_4P_2-CQDs@CdS.

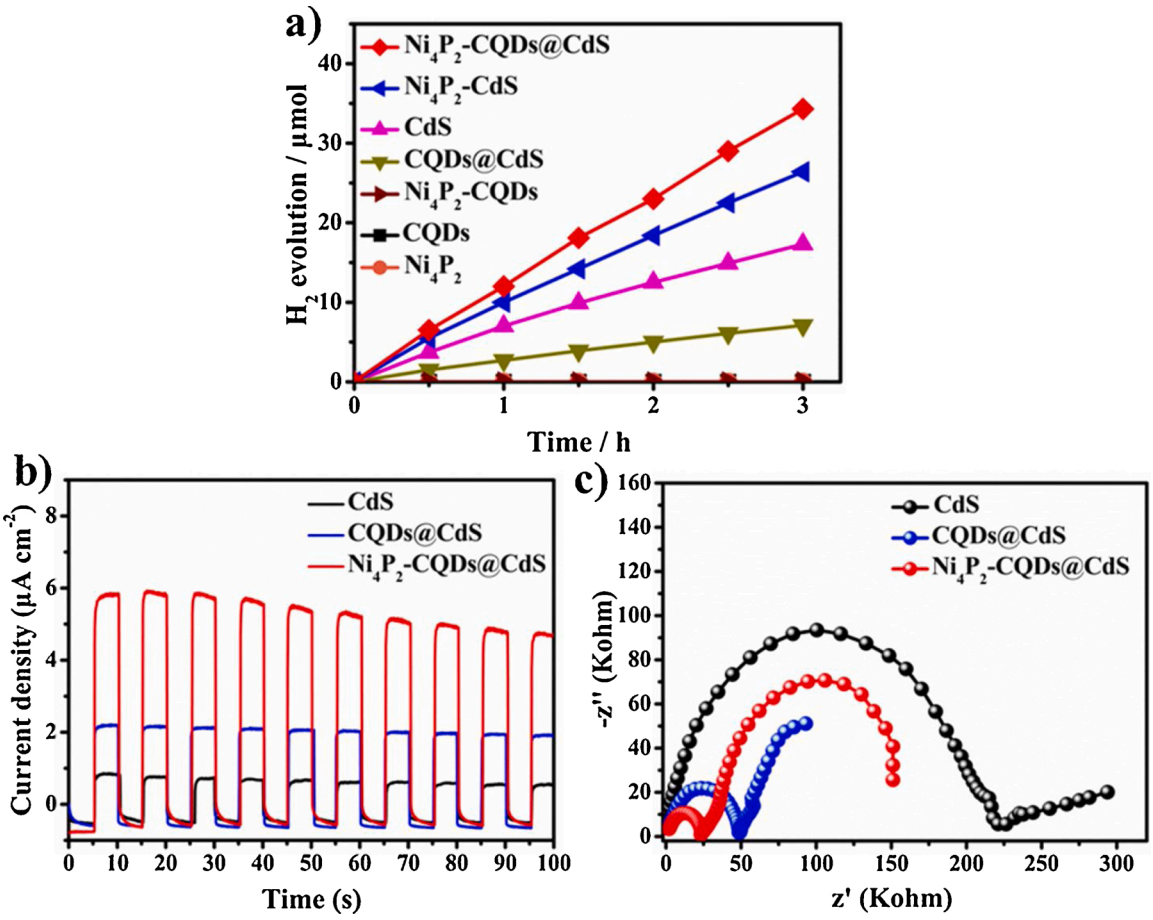

Fig. 8. a) Time course of H_2 evolution in aqueous TEOA solution (10 %, v/v) by different photocatalysts under LED lamp irradiation (λ = 420 nm; 100 mW cm^{-2}). b) Transient photocurrent spectra and c) EIS plots for pure CdS, CQDs@CdS and Ni_4P_2-CQDs@CdS.

circular radius in the impedance spectrum of Ni_4P_2-CQDs@CdS (Fig. 8c) in comparison with those of CdS and CQDs@CdS once again signifies a lowest charge-transfer resistance in the hybrid that ensures the fastest electron transfer. These results of photo/electrochemical studies verify the improved separation and migration of photogenerated charge carriers in Ni_4P_2-CQDs@CdS, thus leading to the good performance of the visible-light-driven water splitting.

A reasonable mechanism of Ni_4P_2-CQDs@CdS for H_2 and H_2O_2 evolutions is proposed based on above results (Fig. 9). For the three components reaction system of Ni_4P_2-CQDs@CdS, once the photocatalytic reaction starts, the CQDs@CdS semiconductor composite will combine with Ni_4P_2 molecular catalyst due to the enrichment effect of CQDs to Ni_4P_2. CQDs are capable of absorbing a longer wavelength visible light and then emit the shorter wavelength light [64,65]. CQDs serve as an electron acceptor, and the photo-induced electrons excited from CdS under visible light shuttle freely to CQDs, thus efficiently retarding the recombination and prolonging the lifetime of electron-hole pairs. Meanwhile, H_2 evolution half-reaction in Fig. 8a confirms that the photoinduced electrons in the conduction band of CdS migrate to CQDs, and then to Ni_4P_2, as well as subsequent proton reduction to form H_2.

The fact of detection of H_2O_2 (Fig. 4a and Fig. S17) proves that the generated holes at the VB of CdS transfer to CQDs and oxidize H_2O to produce H_2O_2. Therefore, in this water splitting system over Ni_4P_2-CQDs@CdS, Ni_4P_2 plays an essential role of reduction sites for H_2 evolution while CQDs contributeoxidation reaction sites for H_2O_2 evolution through a two-electron process (i.e., $2H_2O \rightarrow H_2O_2 + H_2$).

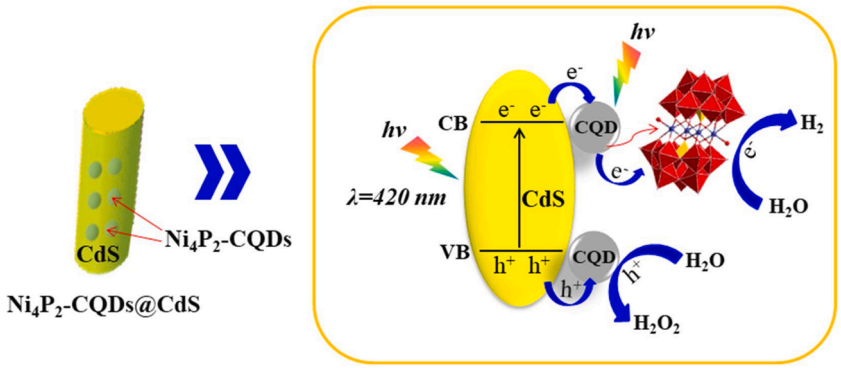

Fig. 9. The proposed mechanism for photocatalytic water splitting of the hybrid Ni_4P_2-CQDs@CdS system.

4. Conclusion

In summary, we successfully demonstrated a novel three component system of Ni_4P_2-CQDs@CdS for water splitting without addition sacrificial agents. This is the first successful strategy for realizing simultaneous generation H_2 and H_2O_2 under visible light irradiation via combining Ni_4P_2 POM catalyst and CQDs@CdS semiconductor composite. The result exhibits the electrons transfer from CdS to CQDs and then to Ni_4P_2, making electrons accumulate in Ni_4P_2 for H_2 evolution. The generated holes at the VB of CdS transfer to CQDs and oxidize H_2O to produce H_2O_2. Under appropriate conditions, a high H_2 formation rate of 145.0 μmol g_{cat}^{-1} h^{-1}, turnover frequency of 15.5 h^{-1} and apparent quantum efficiency ~0.57 % at 420 nm are obtained. The iodometric method detects 0.45 μmol H_2O_2 after irradiation 3 h and the molar ratio of H_2 and H_2O_2 is close to 1:1, indicating the electron/hole utilization ratio is equal. CQDs have multiple roles such as light absorber, electron acceptor and donor, H_2O-to-H_2O_2 reaction sites and Ni_4P_2 POM enrichment center. Besides, the construction of electron transfer direction not only reduces surface charge recombination but also suppresses photocorrosion. Owing to the CQDs over CdS NRs possess the enrichment effect for Ni_4P_2 catalyst, Ni_4P_2-CQDs@CdS exhibits a high H_2 production rate in pure aqueous solution. This work opens up new perspectives for the design and development of efficient multicomponent photocatalysts for overall water splitting.

CRediT authorship contribution statement

Yuanjuan Dong and Qing Han: contributed equally to this paper. **Yuanjuan Dong and Qing Han:** prepared, characterized, tested the catalysts and wrote the paper. **Chunjiang Xu:** offered a help for photoeletrochemical measurements. **Congzhao Dong and Yong Peng:** performed the TEM and TEM-EDS tests. **Qiyu Hu:** helped to revise the paper. **Yong Ding and Yaqian Lan:** supervised the project and wrote the paper.

Declaration of Competing Interest

The authors report no declarations of interest.

Acknowledgements

This work was financially supported by the National Natural Science Foundation of China (Grants Nos. 21773096 and 22075119).

References

[1] M. Grätzel, Photoelectrochemical cells, Nature 414 (2001) 338–344.
[2] N.S. Lewis, Toward cost-effective solar energy use, Science 315 (2007) 798–801.
[3] M. Yagi, M. Kaneko, Molecular catalysts for water oxidation, Chem. Rev. 101 (2001) 21–35.
[4] N. Armaroli, V. Balzani, The future of energy supply: challenges and opportunities, Angew. Chem. Int. Ed. 46 (2007) 52–66.
[5] B. Tian, Y.Q. Wu, G.X. Lu, Metal-free plasmonic boron phosphide/graphitic carbon nitride with coreshell structure photocatalysts for overall water splitting, Appl. Catal. B Environ. 280 (2021), 119410.
[6] F.E. Osterloh, Inorganic nanostructures for photoelectrochemical and photocatalytic water splitting, Chem. Soc. Rev. 42 (2013) 2294–2320.
[7] T. Hisatomi, J. Kubota, K. Domen, Recent advances in semiconductors for photocatalytic and photoelectrochemical water splitting, Chem. Soc. Rev. 43 (2014) 7520–7535.
[8] X.H. Cao, C.J. Xu, X.M. Liang, J.R. Ma, M.E. Yue, Y. Ding, Rationally designed/assembled hybrid $BiVO_4$-based photoanode for enhanced photoelectrochemical performance, Appl. Catal. B: Environ. 260 (2020), 118136.
[9] T. Hisatomi, K. Domen, Reaction systems for solar hydrogen production via water splitting with particulate semiconductor photocatalysts, Nat. Catal. 2 (2019) 387–399.
[10] Z. Zou, J. Ye, K. Sayama, H. Arakawa, Direct splitting of water under visible light irradiation with an oxide semiconductor photocatalyst, Nature 414 (2001) 625–627.
[11] J. Liu, Y. Liu, N. Liu, Y. Han, X. Zhang, H. Huang, Y. Lifshitz, S.T. Lee, J. Zhong, Z. H. Kang, Metal-free efficient photocatalyst for stable visible water splitting via a two-electron pathway, Science 347 (2015) 970–974.
[12] T.R. Cook, D.K. Dogutan, S.Y. Reece, Y. Surendranath, T.S. Teets, D.G. Nocera, Solar energy supply and storage for the legacy and nonlegacy worlds, Chem. Rev. 110 (2010) 6474–6502.
[13] A. Kudo, Y. Miseki, Heterogeneous photocatalyst materials for water splitting, Chem. Soc. Rev. 38 (2009) 253–278.
[14] T. Hisatomi, K. Domen, Particulate photocatalysts for water splitting: recent advances and future prospects, ACS Energy Lett. 4 (2019) 542–549.
[15] Z. Li, L. Zhang, Y. Liu, C. Shao, Y. Gao, F. Fan, J. Wang, J. Li, J. Yan, R. Li, C. Li, Surface-polarity-induced spatial charge separation boosts photocatalytic overall water splitting on GaN nanorod arrays, Angew. Chem. Int. Ed. 59 (2020) 935–942.
[16] J. Wang, A.S. Cherevan, C. Hannecart, S. Naghdi, S.P. Nandan, T. Gupta, D. Eder, Ti-based MOFs: New insights on the impact of ligand composition and hole scavengers on stability, charge separation and photocatalytic hydrogen evolution, Appl. Catal. B Environ. 283 (2021), 119626.
[17] L. Wang, X. Zheng, L. Chen, Y. Xiong, H. Xu, Van der waals heterostructures comprised of ultrathin polymer nanosheets for efficient Z-scheme overall water splitting, Angew. Chem. Int. Ed 57 (2018) 3454–3458.
[18] C.M. Wolff, P.D. Frischmann, M. Schulze, B.J. Bohn, R. Wein, P. Livadas, M. T. Carlson, F. Jäckel, J. Feldmann, F. Würthner, J.K. Stolarczyk, All-in-one visible-light-driven water splitting by combining nanoparticulate and molecular co-catalysts on CdS nanorods, Nat. Energy 3 (2018) 862–869.
[19] Z. Han, F. Qui, R. Eisenberg, P.L. Holland, T.D. Krauss, Robust photogeneration of H_2 in water using semiconductor nanocrystals and a nickel catalyst, Science 338 (2012) 1321–1324.
[20] F. Wen, C. Li, Hybrid artificial photosynthetic systems comprising semiconductors as light harvesters and biomimetic complexes as molecular cocatalysts, Acc. Chem. Res. 46 (2013) 2355–2364.
[21] C.A. Caputo, M.A. Gross, V.W. Lau, C. Cavazza, B.V. Lotsch, E. Reisner, Photocatalytic hydrogen production using polymeric carbon nitride with A hydrogenase and a bioinspired synthetic Ni catalyst, Angew. Chem. Int. Ed. 53 (2014) 11538–11542.
[22] G. Zhao, Y. Sun, W. Zhou, X. Wang, K. Chang, G. Liu, H. Liu, T. Kako, J. Ye, Superior photocatalytic H_2 production with cocatalytic Co/Ni species anchored on sulfide semiconductor, Adv. Mater. 29 (2017), 1703258.
[23] H. Yang, C. Yang, N.N. Zhang, K.L. Mo, Q. Li, K.L. Lv, J.J. Fan, L.L. Wen, Drastic promotion of the photoreactivity of MOF ultrathin nanosheets towards hydrogen production by deposition with CdS nanorods, Appl. Catal. B: Environ. 285 (2021), 119801.
[24] P.D. Tran, L.H. Wong, J. Barber, J.S.C. Loo, Recent advances in hybrid photocatalysts for solar fuel production, Energy Environ. Sci. 5 (2012) 5902–5918.
[25] M.A. Gross, A. Reynal, J.R. Durrant, E. Reisner, Versatile photocatalytic systems for H_2 generation in water based on an efficient dubois-type nickel catalyst, J. Am. Chem. Soc. 136 (2014) 356–366.
[26] W. Zhang, H.L. He, Y. Tian, K. Lan, Q. Liu, C.Y. Wang, Y. Liu, A. Elzatahry, R. C. Che, W. Li, D.Y. Zhao, Synthesis of uniform ordered mesoporous TiO_2 microspheres with controllable phase junctions for efficient solar water splitting, Chem. Sci. 10 (2019) 1664–1670.
[27] Q. Hu, X.Y. Meng, Y.J. Dong, Q. Han, Y.F. Wang, Y. Ding, A stable iron-containing polyoxometalate coupled with semiconductor for efficient photocatalytic water oxidation under acidic condition, Chem. Commun 55 (2019) 11778–11781.
[28] Y.R. Choi, D. Jeon, Y. Choi, J. Ryu, B.S. Kim, Self-assembled supramolecular hybrid of carbon nanodots and polyoxometalates for visible-light-driven water oxidation, ACS Appl. Mater. Interfaces 10 (2018) 13434–13441.
[29] H. Yu, R. Shi, Y. Zhao, G.I.N. Waterhouse, L.Z. Wu, C.H. Tung, T. Zhang, Smart utilization of carbon dots in semiconductor photocatalysis, Adv. Mater. 28 (2016) 9454–9477.
[30] A. Cadranel, J.T. Margraf, V. Strauss, T. Clark, D.M. Guldi, Carbon nanodots for charge-transfer processes, Acc. Chem. Res. 52 (2019) 955–963.
[31] Q. Yin, J.M. Tan, C. Besson, Y.V. Geletii, D.G. Musaev, A.E. Kuznetsov, Z. Luo, K. I. Hardcastle, C.L. Hill, A fast soluble carbon-free molecular water oxidation catalyst based on abundant metals, Science 328 (2010) 342–345.
[32] P. Huang, C. Qin, Z.M. Su, Y. Xing, X.L. Wang, K.Z. Shao, Y.Q. Lan, E.B. Wang, Self-assembly and photocatalytic properties of polyoxoniobates: $\{Nb_{24}O_{72}\}$, $\{Nb_{32}O_{96}\}$, and $\{K_{12}Nb_{96}O_{288}\}$ clusters, J. Am. Chem. Soc. 134 (2012) 14004–14010.
[33] F.Y. Song, Y. Ding, B.C. Ma, C. Wang, Q. Wang, X.Q. Du, S. Fu, J. Song, $K_7[Co^{III}Co^{II}(H_2O)W_{11}O_{39}]$: A molecular mixed-valence keggin polyoxometalate catalyst of high stability and efficiency for visible light-driven water oxidation, Energy Environ. Sci. 6 (2013) 1170–1184.
[34] X.Q. Du, J.L. Zhao, J.Q. Mi, Y. Ding, P.P. Zhou, B.C. Ma, J.W. Zhao, J. Song, Efficient photocatalytic H_2 evolution catalyzed by an unprecedented robust molecular semiconductor {Fe11} nanocluster without cocatalysts at neutral conditions, Nano Energy 16 (2015) 247–255.
[35] B. Schwarz, J. Forster, M.K. Goetz, D. Yücel, C. Berger, T. Jacob, C. Streb, Visible-light-driven water oxidation by a molecular manganese vanadium oxide cluster, Angew. Chem. Int. Ed. 55 (2016) 6329–6333.
[36] X.B. Han, Z.M. Zhang, T. Zhang, Y.G. Li, W. Lin, W. You, Z.M. Su, E.B. Wang, Polyoxometalate-based cobalt–phosphate molecular catalysts for visible light-driven water oxidation, J. Am. Chem. Soc. 136 (2014) 5359–5366.
[37] X.J. Kong, Z. Lin, Z.M. Zhang, T. Zhang, W. Lin, Hierarchical integration of photosensitizing metal–organic frameworks and nickel-containing polyoxometalates for efficient visible-light-driven hydrogen evolution, Angew. Chem. Int. Ed. 55 (2016) 6411–6416.
[38] Z.M. Zhang, T. Zhang, C. Wang, Z. Lin, L.S. Long, W. Lin, Photosensitizing metal organic framework enabling visible-light-driven proton reduction by a wells–dawson-type polyoxometalate, J. Am. Chem. Soc. 137 (2015) 3197–3200.

[39] S. Li, S. Liu, S. Liu, Y. Liu, Q. Tang, Z. Shi, S. Ouyang, J. Ye, {Ta_{12}}/{Ta_{16}} cluster-containing polytantalotungstates with remarkable photocatalytic H_2 evolution activity, J. Am. Chem. Soc. 134 (2012) 19716–19721.
[40] Y. Hu, X. Cao, L. Yu, Y.Y. Wang, J. Ning, S. Xu, X.W. Lou, Carbon-coated CdS petalous nanostructures with enhanced photostability and photocatalytic activity, Angew. Chem. Int. Ed. 52 (2013) 5636–5639.
[41] R. Shi, H.F. Ye, F. Liang, Z. Wang, K. Li, Y. Weng, Z. Lin, W.F. Fu, C.M. Che, Y. Chen, Interstitial P-doped CdS with long-lived photogenerated electrons for photocatalytic water splitting without sacrificial agents, Adv. Mater. 30 (2018), 1705941.
[42] J.M. Clemente-Juan, E. Coronado, J. Galán-Mascarós, C.J. Gómez-García, Increasing the nuclearity of magnetic polyoxometalates. syntheses, structures, and magnetic properties of salts of the heteropoly complexes $[Ni_3(H_2O)_3(PW_{10}O_{39})H_2O]^{7-}$, $[Ni_4(H_2O)_2(PW_9O_{34})_2]^{10-}$, and $[Ni_9(OH)_3(H_2O)_6(HPO_4)_2(PW_9O_{34})_3]^{16-}$, Inorg. Chem. 38 (1999) 55–63.
[43] C.X. Guo, D. Zhao, Q. Zhao, P. Wang, X. Lu, Na^+-functionalized carbon quantum dots: a new draw solute in forward osmosis for seawater desalination, Chem. Commun. 50 (2014) 7318–7321.
[44] B. Wang, S. He, L. Zhang, X. Huang, F. Gao, W. Feng, P. Liu, CdS Nanorods decorated with inexpensive NiCd bimetallic nanoparticles as efficient photocatalysts for visible-light-driven photocatalytic hydrogen evolution, Appl. Catal. B Environ. 243 (2019) 229–235.
[45] H. Peng, J. Travas-Sejdic, Simple aqueous solution route to luminescent carbogenic dots from carbohydrates, Chem. Mater. 21 (2009) 5563–5565.
[46] J. Zhou, C. Booker, R. Li, X. Zhou, T.K. Sham, X. Sun, Z. Ding, An electrochemical avenue to blue luminescent nanocrystals from multiwalled carbon nanotubes (MWCNTs), J. Am. Chem. Soc. 129 (2007) 744–745.
[47] J.H. Deng, Q.J. Lu, N.X. Mi, H.T. Li, M.L. Liu, M.C. Xu, L. Tan, Q.J. Xie, Y.Y. Zhang, S.Z. Yao, Electrochemical synthesis of carbon nanodots directly from alcohols electrochemical synthesis of carbon nanodots, Chem. Eur. J. 20 (2014) 4993–4999.
[48] S. Wang, B.Y. Guan, X. Wang, X.W.D. Lou, Toward noble-metal-free visible-light-driven photocatalytic hydrogen evolution: monodisperse Sub-15 nm Ni_2P nanoparticles anchored on porous g-C_3N_4 nanosheets to engineer 0D-2D heterojunction interfaces, J. Am. Chem. Soc. 140 (2018) 15145–15148.
[49] H.W. Tseng, M.B. Wilker, N.H. Damrauer, G. Dukovic, Charge, transfer dynamics between photoexcited CdS nanorods and mononuclear Ru water-oxidation catalysts, J. Am. Chem. Soc. 135 (2013) 3383–3386.
[50] J. Chen, X.J. Wu, L. Yin, B. Li, X. Hong, Z. Fan, B. Chen, C. Xue, H. Zhang, One-pot synthesis of CdS nanocrystals hybridized with single-layer transition-metal dichalcogenide nanosheets for efficient photocatalytic hydrogen evolution, Angew. Chem. Int. Ed 54 (2015) 1210–1214.
[51] C. Eley, T. Li, F. Liao, S.M. Fairclough, J.M. Smith, G. Smith, S.C.E. Tsang, Nanojunction-mediated photocatalytic enhancement in heterostructured CdS/ZnO, CdSe/ZnO, and CdTe/ZnO nanocrystals, Angew. Chem. Int. Ed 53 (2014) 7838–7842.
[52] X. Fu, L. Zhang, L. Liu, H. Li, S. Meng, X. Ye, S. Chen, In situ photodeposition of MoS_x on CdS nanorods as a highly efficient cocatalyst for photocatalytic hydrogen production, J. Mater. Chem. A 5 (2017) 15287–15293.
[53] S.S. Yi, J.M. Yan, B.B. Wulan, S.J. Li, K.H. Liu, Q. Jiang, Noble-metal-free cobalt phosphide modified carbon nitride: an efficient photocatalyst for hydrogen generation, Appl. Catal. B: Environ. 200 (2017) 477–483.
[54] X.J. Kong, Z.K. Lin, Z.M. Zhang, T. Zhang, W.B. Lin, Hierarchical integration of photosensitizing metal-organic frameworks and nickel-containing polyoxometalates for efficient visible-light-driven hydrogen evolution, Angew. Chem. Int. Ed. 128 (2016) 6521–6526.
[55] W. Che, W.R. Cheng, T. Yao, F.M. Tang, W. Liu, H. Su, Y.Y. Huang, Q.H. Liu, J. K. Liu, F.C. Hu, Z.Y. Pan, Z.H. Sun, S.Q. Wei, Fast photoelectron transfer in (C_{ring})-C_3N_4 plane heterostructural nanosheets for overall water splitting, J. Am. Chem. Soc. 139 (2017) 3021–3026.
[56] W.J. Sun, X.Y. Meng, C.J. Xu, J.Y. Yang, X.M. Liang, Y.J. Dong, C.Z. Dong, Y. Ding, Amorphous CoO_x coupled carbon dots as a songy porous bifunctional catalyst for efficient photocatalytic water oxidation and CO_2 reduction, Chin. J. Catal. 41 (2020) 1826–1836.
[57] C. Xia, S. Back, S. Ringe, K. Jiang, F.H. Chen, X.M. Sun, S. Siahrostami, K. Chan, H. T. Wang, Confined local oxygen gas promotes electrochemical water oxidation to hydrogen peroxide, Nat. Catal. 3 (2020) 125–134.
[58] J.W. Huang, Y. Zhang, Y. Ding, Rationally designed/constructed CoO_x/WO_3 anode for efficient photoelectrochemical water oxidation, ACS Catal. 7 (2017) 1841–1845.
[59] F. Xue, Y.T. Si, M. Wang, M.C. Liu, L.J. Guo, Toward efficient photocatalytic pure water splitting for simultaneous H_2 and H_2O_2 production, Nano Energy 62 (2019) 823–831.
[60] Y.J. Fu, C.A. Liu, M.L. Zhang, C. Zhu, H. Li, H.B. Wang, Y.X. Song, H. Huang, Y. Liu, Z.H. Kang, Photocatalytic H_2O_2 and H_2 generation from living chlorella vulgaris and carbon micro particle comodified g-C_3N_4, Adv. Energy Mater. (2018), 1802525.
[61] H.J. Li, Y.Y. Gao, Y. Zhou, F.T. Fan, Q.T. Han, Q.F. Xu, X.Y. Wang, M. Xiao, C. Li, Z. G. Zou, Construction and nanoscale detection of interfacial charge transfer of elegant Z-scheme $WO_3/Au/In_2S_3$ nanowire arrays, Nano Lett. 16 (2016) 5547–5552.
[62] X.M. Ning, Y.L. Wu, X.F. Ma, Z. Zhang, R.Q. Gao, J. Chen, D.L. Shan, X.Q. Lu, A novel charge transfer channel to simultaneously enhance photocatalytic water splitting activity and stability of CdS, Adv. Funct. Mater. 29 (2019), 1902992.
[63] R. Chen, Z.H. Yan, X.J. Kong, L.S. Long, L.S. Zheng, Integration of lanthanide–transition–metal clusters onto CdS surfaces for photocatalytic hydrogen evolution, Angew. Chem. Int. Ed. 57 (2018) 16796–16800.
[64] Q. Liu, T.X. Chen, Y.R. Guo, Z.G. Zhang, X.M. Fang, Ultrathin g-C_3N_4 nanosheets coupled with carbon nanodots as 2D/0D composites for efficient photocatalytic H_2 evolution, Appl. Catal. B Environ. 193 (2016) 248.
[65] D. Gogoi, R. Koyani, A.K. Golder, N.R. Peela, Enhanced photocatalytic hydrogen evolution using green carbon quantum dots modified 1-D CdS nanowires under visible light irradiation, Sol. Energy 208 (2020) 966–977.